Available online at www.sciencedirect.com
ScienceDirect
Applied Acoustics 69 (2008) 1258–1269
applied acoustics
www.elsevier.com/locate/apacoust

Numerical investigation on radiation characteristics of discrete-frequency noise from scarf and scoop aero-intakes

Yonghwan Park [a], Sungtae Kim [a], Soogab Lee [a,*], Cheolung Cheong [b]

[a] School of Mechanical Engineering, College of Engineering, Seoul National University, Seoul 151-742, Republic of Korea
[b] School of Mechanical Engineering, College of Engineering, Pusan National University, Pusan 609-735, Republic of Korea

Received 26 March 2007; received in revised form 3 August 2007; accepted 27 September 2007

Abstract

Numerical studies have been carried out to investigate the detailed geometrical effects of full three-dimensional aero-intakes on the radiation of the discrete-frequency rotor–stator interaction noise. The near-field acoustic radiation characteristics and the far-field directivity patterns from the scarf and scoop aero-intakes with three different scarf/scoop angles are quantitatively analyzed and compared. The near-field predictions were obtained by solving the linearized Euler equations with computational aeroacoustic techniques consisting of high-order finite difference scheme, non-reflecting boundary conditions, overset grids and parallel computational methods. For the prediction of far-field directivity pattern, the Kirchhoff integral method was applied. By comparing the directivities of discrete-frequency noise radiating from the scarf and the scoop aero-intakes with that from an axisymmetric aero-intake, it is shown that the 7 dB noise reduction at downward peak radiation angle can be achieved by using the scoop aero-intake with scoop angle of 15°, and the 5 dB noise reduction by the scarf aero-intake with the scarf angle of 15°. The scattering of the radiating acoustic wave by the background mean flow around the aero-intakes shifts the peak lobe radiation angle toward ground and increases the amplitude of the acoustic pressure compared with the cases without mean flow effect. Overall, the scoop aero-intake was found to be more effective than the scarf and the axisymmetric aero-intakes in view of the lower noise radiation toward ground.

JEL classification: Original Research paper; 300; 310; 350

Keywords: Scarf aero-intake; Scoop aero-intake; Computational aeroacoustics; Turbo-fan engine noise; Rotor–stator interaction noise

1. Introduction

In general, aircraft noises are categorized into airframe noise, jet noise and engine noise according to the noise generation mechanism. Among them, jet noise was a dominant noise source for past decades. Recently, the increase in engine size with larger bypass-ratio makes fan noise be a dominant noise source, especially during take-off and landing. The fan noise is known to be composed of broadband noise due to turbulence–fan interaction and discrete-frequency noise such as rotor–stator interaction noise which is generally accepted as one of the principal noise sources for fans with subsonic tip speeds [1].

In order to reduce the fan noise, so-called passive control methods such as surface treatments and re-direction methods have been used in commercial aero-engines. The former dissipates an acoustic energy while the latter diverts the propagating direction of the acoustic wave from aero-intakes. The passive control methods are schematically illustrated in Fig. 1. The elliptical aero-inlets, the scarf, and the scoop aero-intakes have been proposed to reduce community exposure to aircraft noise, by diverting forward arc engine noise away from the ground [2]. Compared with surface treatment method, the re-direction of noise propagation by the scarf and the scoop aero-intakes can

* Corresponding author. Tel.: +82 2 880 7384; fax: +82 2 875 4360.
E-mail address: solee@snu.ac.kr (S. Lee).

0003-682X/$ - see front matter © 2007 Elsevier Ltd. All rights reserved.
doi:10.1016/j.apacoust.2007.09.005

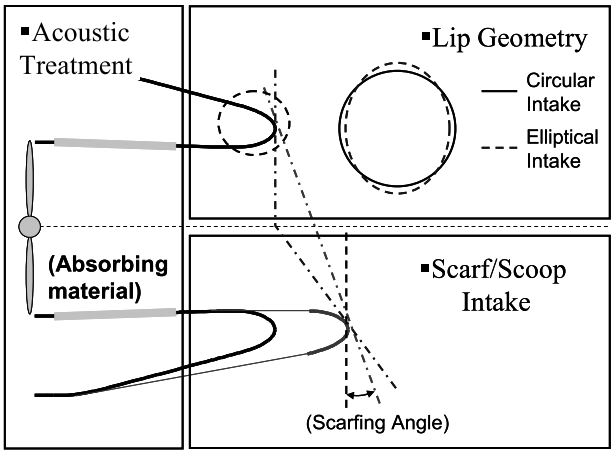

Fig. 1. Various methods for the reduction of noise propagation toward ground.

attain the same noise reduction effect while retaining the shorter, lighter and structurally simpler aero-intake [3].

Fig. 2 presents the typical negative scarf and scoop aero-intakes [4]. The scarf aero-intake has a constant scarf angle along the circumferential direction (transition angle is 180°; here the transition angle is defined as a circumferential angle of the region where the scarf angle is not zero) while the scoop aero-intake has an inconstant scarf angle (transition angle is less than 180°). Thus, the scoop aero-intake may be considered to be a compromise between the axisymmetric aero-intake and the scarf aero-intake. More specifically, the scarf aero-intakes are divided into the negative (lower-side forward-extended type) and the positive (upper-side forward-extended type) by the position of the extended side. The positive scarf aero-intake has better aerodynamic performance than negative one, but at the same time, it has bad characteristics in that more sound propagates toward ground where most of noise regulations are applied.

Experimental studies [2,3,5] showed that the scarf and the scoop intakes have a significant impact on the radiation characteristics of intake sound including its far-field directivity pattern. For the case of broadband noise radiation, it is reported that the peak SPL (sound pressure level) is reduced by about 6–8 dB (decibel) with the negative scarf aero-intake of a scarf angle of 15° [5].

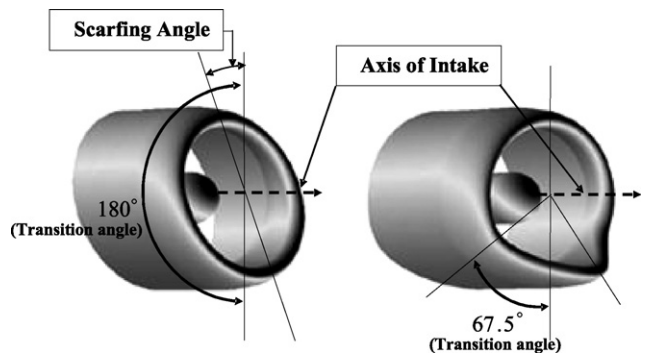

Fig. 2. Typical geometries of scarf (left) and scoop aero-intake (right)[4].

Theoretical study was implemented by Keith and Peake [6]. Their investigation was based on the so-called geometrical theory of diffraction method, and gave a reasonable result. However, this theoretical approach is restricted to simple geometries and flow conditions, and thus may be difficult to be applied in real situations.

In this respect, numerical methods are better suited for the analysis of sound radiation characteristics from realistic three-dimensional aero-engines such as the scarf and the scoop aero-intakes with surface treatments. Some numerical studies [7,8] have been carried out to investigate the radiation characteristics of acoustic wave from aero-intakes. However, these studies have been performed only with axisymmetric aero-intakes, i.e., relatively simple geometries.

In this paper, we carried out numerical studies to investigate the detailed geometrical effects of full three-dimensional aero-intakes such as the scarf and the scoop aero-intakes on the radiation of the discrete-frequency rotor–stator interaction noise. To predict the sound field accurately and effectively, the computational aeroacoustic techniques are utilized. Low dispersion/dissipation high-order schemes are used for the accurate simulation of near-field acoustic propagation. To model the three-dimensional complex geometries of the scarf and the scoop aero-intakes with good-quality mesh over whole computation domain, the overset grid technique is applied with high-order interpolation methods [9], which was already applied for the different applications [10,11]. Although the performance of computer hardware has been dramatically improved, the computational cost for the noise prediction of full three-dimensional realistic aero-engine is still high. Therefore, present numerical methods are based on parallel computing techniques to reduce the computation time, which may allow the present method to be used as a design tool for low-noise aero-intakes. The Kirchhoff integral methods [12–15] are used to effectively predict very far acoustic fields.

The main target of this article is to investigate the effect of the detailed geometries of scarf and the scoop aero-intakes on the radiation characteristics of the discrete-frequency rotor–stator interaction noise. By comparing the directivities of discrete-frequency noise radiating from an axisymmetric aero-intake with those from the scarf and the scoop aero-intakes with various scarf/scoop angles, the noise reduction which can be achieved by using the scarf and the scoop aero-intakes is quantitatively assessed. In addition, the effect of the mean flow on the noise exposure into the ground direction is evaluated by comparing the directivities of discrete-frequency noise through the scarf and the scoop aero-intakes with and without mean flow.

The outline of this article is as follows. First, the governing equations and the numerical methods including discretization methods, boundary conditions, overset grid technique, the Kirchhoff method, and the parallel computations are provided in Section 2. The numerical methods

are validated with two benchmark problems in Section 3. Numerical predictions and their analysis on the near-field and far-field radiation characteristics of acoustic waves from the axisymmetric, the scarf and the scoop aero-intakes with and without mean flows are provided in Section 4. The conclusion of this work is then presented in Section 5.

2. Governing equations and numerical methods

2.1. Governing equations

In the down-stream region of aero-engines, the instability waves may be generated by the interaction of acoustic wave with shear flow [10]. In the engine inlet, however, these instability waves are not a dominant factor to the flow characteristics. In addition, it can be assumed that wave propagation itself is hardly affected by viscosity and the contribution of sound perturbation to the convection velocity of flow is negligible. With the above assumptions, therefore, sound propagation can be described by solving linearized Euler equations. The conservative form of non-dimensionalized governing equations in the cylindrical coordinates is

$$\frac{\mathbf{Q}_l}{t}+\frac{\mathbf{E}_l}{x}+\frac{\mathbf{F}_l}{r}+\frac{1}{r}\frac{\mathbf{G}_l}{\theta}+\frac{\mathbf{H}_l}{r}+\mathbf{M}_l=0, \tag{1}$$

where,

$$\mathbf{Q}_l=\begin{pmatrix}\rho'\\ \rho_0u'\\ \rho_0v'\\ \rho_0w'\\ \rho_0e'\end{pmatrix},\quad \mathbf{E}_l=\begin{pmatrix}\rho_0u'+\rho'u_0\\ \rho_0u_0u'+p'\\ \rho_0u_0v'\\ \rho_0u_0w'\\ (\rho_0e'+p')u_0+p_0u'\end{pmatrix},$$

$$\mathbf{F}_l=\begin{pmatrix}\rho_0v'+\rho'v_0\\ \rho_0v_0u'\\ \rho_0v_0v'+p'\\ \rho_0v_0w'\\ (\rho_0e'+p')v_0+p_0v'\end{pmatrix},$$

$$\mathbf{G}_l=\begin{pmatrix}\rho_0w'+\rho'w_0\\ \rho_0w_0u'\\ \rho_0w_0v'\\ \rho_0w_0w'+p'\\ (\rho_0e'+p')w_0+p_0w'\end{pmatrix},$$

$$\mathbf{H}_l=\frac{1}{r}\begin{pmatrix}\rho_0v'+\rho'v_0\\ \rho_0v_0u'\\ \rho_0v_0v'-2\rho_0w_0w'-\rho'w_0^2\\ 2\rho_0v_0w'+\rho_0v'w_0+\rho'v_0w_0\\ (\rho_0e'+p')v_0+p_0v'\end{pmatrix}\text{ and}$$

$$\mathbf{M}_l=\begin{pmatrix}0\\ (\rho_0u'+\rho'u_0)\frac{u_0}{x}+(\rho_0v'+\rho'v_0)\frac{u_0}{r}+(\rho_0w'+\rho'w_0)\frac{1}{r}\frac{u_0}{\theta}\\ (\rho_0u'+\rho'u_0)\frac{v_0}{x}+(\rho_0v'+\rho'v_0)\frac{v_0}{r}+(\rho_0w'+\rho'w_0)\frac{1}{r}\frac{v_0}{\theta}\\ (\rho_0u'+\rho'u_0)\frac{w_0}{x}+(\rho_0v'+\rho'v_0)\frac{w_0}{r}+(\rho_0w'+\rho'w_0)\frac{1}{r}\frac{w_0}{\theta}\\ (\rho_0u'+\rho'u_0)\frac{e_0}{x}+(\rho_0v'+\rho'v_0)\frac{e_0}{r}+(\rho_0w'+\rho'w_0)\frac{1}{r}\frac{e_0}{\theta}\end{pmatrix}.$$

Here, $\mathbf{Q}_l$ is the unknown vector, $\mathbf{E}_l$, $\mathbf{F}_l$ and $\mathbf{G}_l$ are the linear flux vectors, $\mathbf{H}_l$ is the source vector, and $\mathbf{M}_l$ is the mean flow gradient vector. $\mathbf{M}_l$ consists of the mean flow gradient terms and are equal to zero when mean flow is uniform. In Eq. (1), the lower letter, 0, denotes the quantity related to steady mean flow and the upper letter ($'$), presents its perturbation. In the present study, the length scales are non-dimensionalized by a radius of intake, r_a, the velocity scales by a speed of sound, c_∞, the time scales by r_a/c_∞ density scales by ρ_∞, and the pressure scales by$\rho_\infty c_\infty^2$.

2.2. Numerical methods

Fig. 3 summarizes the procedure of current numerical methods for the prediction of noise radiation from aero-intakes. Firstly, acoustic sources induced by the rotor–stator interaction are modeled by the Tyler and Sofrin theory at fan-face [16]. Then near-field acoustic solutions are computed by solving the linearized Euler equations with computational aeroacoustics techniques such as high-order discretization schemes, non-reflecting boundary conditions, overset grids and parallel computing techniques. In this stage, the fourth-order DRP (dispersion-relation-preserving) scheme is employed for the spatial derivative, the third-order explicit Adams–Bashforth method is used for the time integration and the artificial selective damping is adopted for the elimination of spurious waves [17]. Finally, in order to predict the far-field acoustic information and the directivity pattern, the predicted near-field data around the aero-intake are utilized for the Kirchhoff integral method. The detailed descriptions on the boundary conditions, overset grid techniques, parallel computing and the Kirchhoff formulation are given below.

2.2.1. Boundary conditions

Fig. 4 presents the whole computation domain with applied boundary conditions. Since the computational domain is usually finite, boundary conditions must be imposed on the edge of the grid. These boundary conditions can generate undesirable spurious fluctuations.

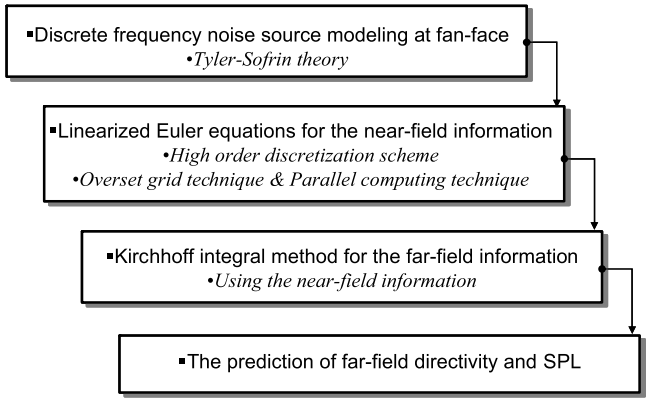

Fig. 3. Schematics of present numerical methods.

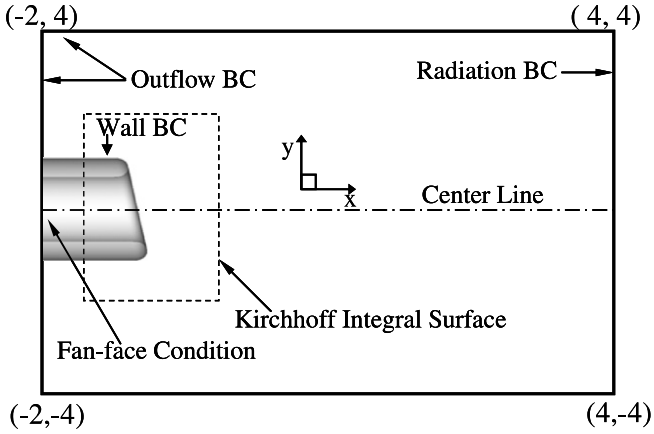

Fig. 4. Whole computation domain with boundary conditions applied.

Therefore, accurate nonreflecting boundary conditions are necessary for computational aeroacoustics.

Boundary condition at fan-face must play two roles at once; one is generating the specific acoustic sources and the other is non-reflecting the back-coming waves from the edge of duct. It is reported that there is no significant effect of the scarf aero-intake on the fan source noise levels for both tones and broadband [5]. Therefore acoustic source modeling for the axisymmetric circular duct at the fan-face can be applied to the simulations for the scarf and the scoop aero-intake. The detailed formulations for modeling the rotor–stator interaction noise and the fan-face condition are given in Refs. [16,18]. The radiation and outflow boundary conditions of Tam and Dong [19] are used as the non-reflecting boundary conditions for the far-field boundaries.

For inviscid flows, the well-known boundary condition at a solid wall is that the velocity components normal to the wall must be equal to zero. This condition is sufficient to determine a unique solution to the Euler equations. For a high-order finite difference scheme, the order of the difference equations is higher than that of the Euler equations. Thus, the zero normal velocity boundary condition is insufficient for determining a unique solution. Therefore, additional numerical constraints must be imposed [20]. Here, the ghost value of pressure was used as the extraneous boundary condition.

2.2.2. Overset grid technique and grid structure

As mentioned above, it is difficult and elaborate to model a complex engine geometry by using one block grid system. Besides, as the scarf and the scoop aero-intakes are geometrically asymmetric, it requires the use of a full three-dimensional grid system. Therefore, to settle this geometrical problem with grid retaining the uniform resolution over the whole computation domain, the overset grid technique connected with a high-order interpolation is applied for the mesh of the aero-intakes.

Fig. 5 shows the overset grid structure that was used for the prediction of the noise propagation from the scarf aero-intake with finite thickness. It consists of two parts; the body-fitted grid over the engine nacelle and background Cartesian grid. To show how well the finite difference scheme resolves the acoustic wave with given Cartesian mesh, there is an index, so-called, the critical wave numbers which are the maximum resolvable wave numbers defined as $|\overline{\alpha_c x} - \alpha x| < 0.005$ (this number may depend on applications), which has the corresponding minimum critical grid points per wavelength (PPW). As the PPW increases for the given schemes, the accuracy is also augmented but the computation time is also increased. Therefore a compromise between the accuracy and the computation time is generally required, especially more important for the three-dimensional simulations as this case. Based on theoretical analysis of the critical wave numbers of DRP schemes [21,22], we set the minimum PPW to be 6. For example, for 10th circumferential mode, $10 \times 6 = 60$, 60 grid point are required at least. The used grids are a H-type rectangular grids with $130(x) \times 100(r) \times 97(\theta)$ in the background block and $200(x) \times 16(r) \times 97(\theta)$ in body-fitted block. The number of circumferential grid size is retained for all of the cases: the axisymmetric, the scarf, the scoop aero-intakes and JT15D [23] aero-intake for the validation.

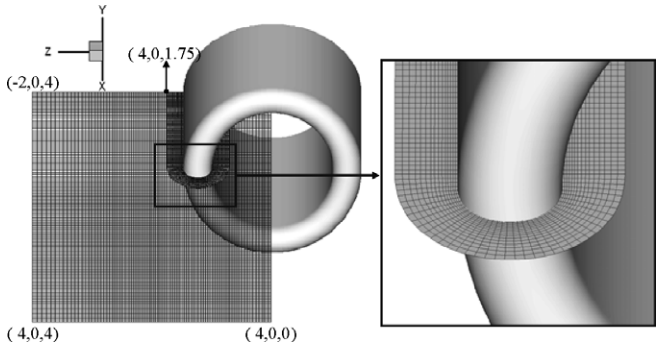

Fig. 5. Grid structure (body-fitted and background grid).

2.2.3. Kirchhoff integral method

To predict the far-field directivity of acoustic wave from aero-engine, the Kirchhoff integral method [12–15] is utilized. The Kirchhoff integral method is based on the application of the wave equation between a known acoustic surface, S, and a point in space within a uniform field. The surface including the noise source is assumed to contain all mean flow effects and possible non-linearities. This method allows the acoustic pressure at a single point in far-field to be predicted by using a known sound field, and therefore, is useful when acoustic near-field is already known. The Kirchhoff integral formula is as follows;

$$p'(\mathbf{x},t) = \frac{1}{4\pi}\iint_s \left[\frac{E_1}{R(1-M_R)} + \frac{E_2}{R(1-M_R)} + \frac{E_3}{R^2(1-M_R)}\right]_{\tau_e} \times \mathrm{d}S(\mathbf{y},\tau_e), \quad (2)$$

where $M = |\mathbf{M}|$, $R = |\mathbf{R}|$, $\mathbf{R} = \mathbf{x} - \mathbf{y}(\tau)$, $\mathbf{x} = x_1\mathbf{i} + x_2\mathbf{j} + x_3\mathbf{k}$, $\mathbf{y} = y_1\mathbf{i} + y_2\mathbf{j} + y_3\mathbf{k}$, $M_R = \mathbf{M}\cdot\mathbf{R}/R$ and $E_1 = -\mathbf{n}\cdot\nabla p' +$

$(\mathbf{M}\cdot\mathbf{n})\,(\mathbf{M}\cdot\nabla p')$, $E_2 = \left[\frac{\cos\varphi - \mathbf{M}\cdot\mathbf{n}}{c_\infty(1-M_R)} - \frac{\mathbf{M}\cdot\mathbf{n}}{c_\infty}\right]\frac{p'}{\tau_e}$ and $E_3 = \left[\frac{1-M^2}{(1-M_R)^2}\right](\cos\varphi - \mathbf{M}\cdot\mathbf{n})p'$. Here, $\mathbf{M}$ is the Mach number vector at which the surface travels, p' is the acoustic pressure $(\mathbf{x}, t)$ denotes the observer's location and time, x_1 is the observer distance vector component which is aligned with the free stream Mach number $\mathbf{M}$, x_2 and x_3 are the transverse components $(\mathbf{y}, \tau_e)$ are the source location and emission time variable, φ is the angle between the normal vector $(\mathbf{n})$ on the Kirchhoff surface and the radiation vector $(\mathbf{R})$, and R is the distance between an observer and a source at the emission time. The emission time including the mean flow effect is given by

$$\tau_e = t - R_e/c_\infty, \tag{3}$$

where,

$$R_e = \frac{-(x_1 - y_1)M + \overline{R}}{\beta^2}, \tag{4}$$

and $\beta^2 = 1 - M^2$, $\overline{R} = \sqrt{(x_1-y_1)^2 + \beta^2(x_2-y_2)^2 + \beta^2(x_3-y_3)^2}$.

2.2.4. Parallel computation

As with many CAA and CFD approaches required excessive computational cost, parallelization offers an effective approach to enable substantial reduction in simulation time for the effective computation of aero-intake noise. To this end, physical domain is divided into several sub-domains by using DDT (domain decomposition technique). The physical domain is split into eight subsections along the circumferential direction, and the each sub-section is split again into two sub-domains along the axial direction of the aero-intake. The calculation code is implemented on parallel computer systems using the message-passing programming model and MPI (message-passing interface) library [24]. The computation was carried out by using 16 processors on the Linux PC cluster which is based on Intel×86 system and Beowulf project [25].

3. Validation of present numerical techniques

In order to assure the numerical stability and to validate the current numerical approaches, the numerical simulation was carried out for the test problem which is the prediction of the directivity of JT15D engine. As mentioned previous, to achieve a high quality numerical solution, an artificial selective damping term was adopted at each grid point. In addition, in DRP scheme, for the numerical stability, the maximum integral time step, Δt_{max} is given by [26]

$$t_{max} = \frac{0.4}{1.75[M + (1 + (x/y)^2)^{0.5}]}\frac{x}{a_0}.$$

where M is a Mach number, a_0 is a speed of sound and Δx, Δy is the least grid spacing in the x, y-direction. To ensure numerical stability it is sufficient to restrict Δt to less than Δt_{max}. In present study, the least Δx is 0.04, the least Δy $(\Delta y = \Delta z)$ is 0.00163625, Δt_{max} is 0.00037, and the used integral time step Δt is 0.0001.

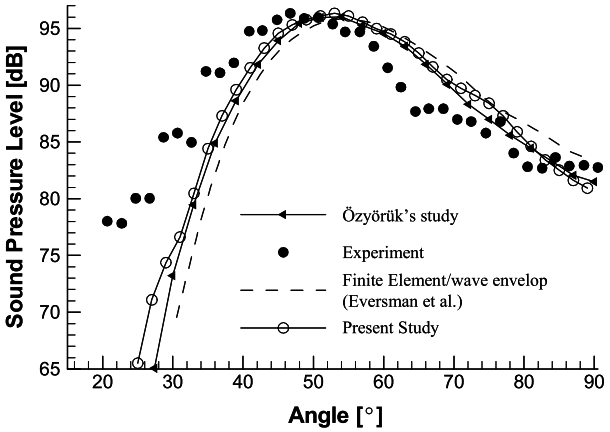

Fig. 6. Comparison of present numerical predictions for the noise radiation from JT15D aero-intake with other numerical and experimental results.

For the numerical validation of present numerical methods, the predicted directivity of JT15D is compared with the experiment and other numerical results [27,28]. Here, the angular frequency (ω) is 18.65 and the excited acoustic mode (m, μ) is (13, 0); m is circumferential mode order and μ is radial mode order. The free stream Mach number M_∞ is -0.204. As seen in Fig. 6, the directivity predicted with the present numerical method has good agreements with the others.

4. Numerical results

In this section, we investigate the effect of the detailed geometries of the scarf and the scoop aero-intakes on the radiation characteristics of the discrete-frequency rotor–stator interaction noise. Firstly, we analyze the basic characteristics of noise propagation through the scarf aero-intake with zero thickness. Here, 'zero thickness' means that the wall thickness of aero-intake is zero. Then, by comparing the directivities of discrete-frequency noise radiating from an axisymmetric aero-intake with that from the scarf and the scoop aero-intakes with finite thickness, the noise reductions which can be achieved with the scarf and the scoop aero-intakes are quantitatively investigated. The effect of the mean flow on the noise propagation is also evaluated by comparing the directivities of discrete-frequency noise from the scarf and scoop aero-intakes with and without mean flow.

4.1. The scarf aero-intake with zero thickness

Fig. 7 shows the instantaneous pressure contour for zero thickness aero-intake with the scarf angle of 10°. The excited acoustic mode (m, μ) is (3, 0) and the angular frequency is 6.5. The mean flow is not considered, namely, $M_\infty = 0$. Fig. 7a shows the instantaneous pressure contour

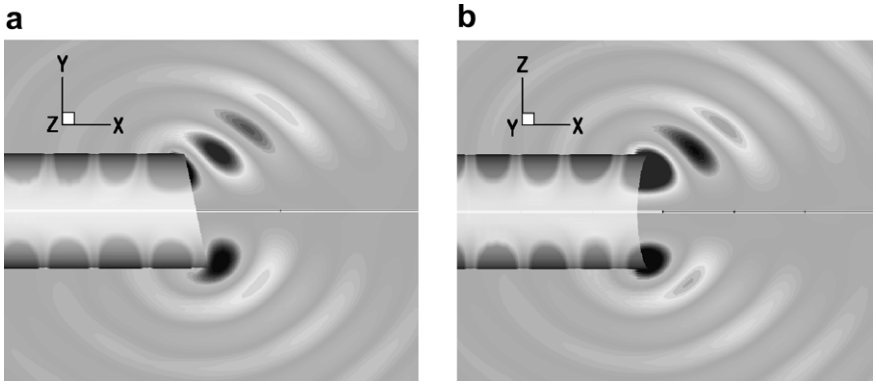

Fig. 7. Predicted acoustic pressure contours from scarf aero-intake with zero thickness: (a) at vertical plane (x–y plane) and (b) at horizontal plane (x–z plane).

at the vertical plane. It shows that the magnitude of downward propagating acoustic wave is lower than that of the upward propagation. Suppose that there is no loss in acoustic energy propagating from given noise source through the aero-intake, it means that the scarf aero-intake decrease the absolute value of acoustic energy propagating downward, i.e., into ground, where most of the environmental noise regulations is concerned. In this respect, it can be inferred that the scarf aero-intake has better radiation characteristics than axisymmetric aero-intake.

Fig. 7b shows the instantaneous pressure contour at the horizontal plane. Although the geometry of the aero-intake is symmetric in the horizontal plane, the acoustic pressure contour is non-symmetric, similar to the acoustic pressure contour in the vertical plane. The reason for this is that the propagation characteristic on horizontal plane is determined by the diffraction effects due to the interaction of swirling acoustic modes with the edge of the aero-intake. More detailed explanation is presented in the next section.

4.2. The scarf and scoop aero-intakes with finite thickness

In the previous section, the noise propagation characteristics from the scarf aero-intake with zero thickness were investigated. However, it is the ideal case chosen for illustrating the basic characteristics of the scarf aero-intake. In this part, the propagation characteristics of acoustic waves from the scarf, the scoop, and the axisymmetric aero-intakes with a finite thickness are analyzed.

Fig. 8 shows the geometries of the scarf and scoop aero-intakes selected for the comparison in the present study. The thickness of the duct wall is the half of the inner radius of the aero-intakes. The cross-section of the aero-intake edge is a circle. As shown in Fig. 8, the transition angle of the scarf aero-intake is 180° and that of the scoop aero-intake is set to be 90°.

Fig. 9 defines the coordinate vector ($\mathbf{R}_{ob}$, φ_{ob}) of the observing points where the far-field directivity is predicted, and presents the geometric parameters for the scarf and the scoop angles: θ_{scarf}; θ_{scoop}. The center position can be defined regardless of the shapes of aero-intakes, which is

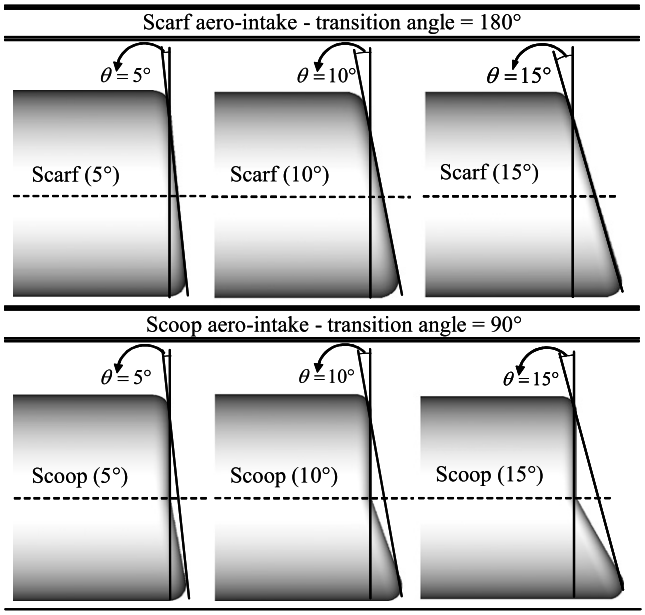

Fig. 8. Geometries of scarf and scoop aero-intakes selected for the present study.

the center of the cross-section of the ducts. R_{ob} denotes the distance between the center point and the far-field observing position. The angle, φ_{ob}, represents an angle between $\mathbf{R}_{ob}$ and an axis of aero-intake. R_{ob} is set to be $115 \times r_a$ in all of the following computations. The scoop angle, θ_{scoop}, can be expressed as the function of the scarf angle, θ_{scarf}, as follows:

$$\theta_{scoop} = \tan^{-1}(2\tan(\theta_{scarf})) \tag{5}$$

In the present study, seven cases of the aero-intake shapes: the axisymmetric aero-intake, the scarf aero-intake with scarf angles of 5°, 10° and 15°, and the scoop aero-intake with scoop angles of 5°, 10° and 15° were numerically analyzed. All of the aero-engines are assumed to have an array of 41 stators in front of the 28-blade rotors, which produce the circumferential mode (13, 0) at the fundamental BPF [27]. The angular frequency (ω) is 18.7.

Fig. 10 shows the predictions for instantaneous acoustic pressure at the plane, $x = d$, from the center point and at

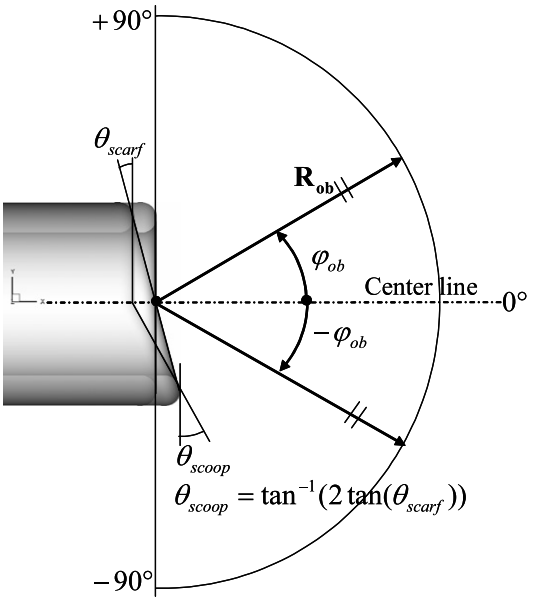

Fig. 9. Definition of each parameter for the Kirchhoff integral.

time $T = 12.5$. The left and right figures present the results for the cases of the scarf and the scoop angles of 10° and 15°, respectively. It can be clearly seen that the number of the peaks (or the valley) of the swirling acoustic pressure at the plane is 13, which equals to the number of excited acoustic modes. We can also see that, in the lower region, the amplitudes of the acoustic pressure for the cases of the scarf and scoop angles of 15° are lower than those of 10°.

Fig. 11 shows the isobars of acoustic pressure from the axisymmetric, the scarf (15°) and the scoop (15°) aero-intakes. As expected, the acoustic wave radiating from the axisymmetric aero-intake is symmetric along the circumferential direction. On the other hand, acoustic waves from the scarf (15°) and the scoop (15°) aero-intakes are found to be weakened in the downward ($-y$)-direction. On the horizontal direction ($\pm z$-direction), more intense sound from the scoop (15°) propagates compared with that of the scarf (15°), which means that the scoop gives the least noise in the downward direction. This result may be explained by using the Keller's diffraction cone [29]. Fig. 12 shows the physical characteristics of acoustic wave diffraction for three cases. Wave diffractions are produced by the incident ray which encounters the edge of the aero-intake. As the ray of acoustic wave meets the edge of the aero-intake, Keller's cones of diffracted ray are produced, and determine the structure of the radiation field [6,29]. In Fig. 12, each point on the edge of aero-intake is

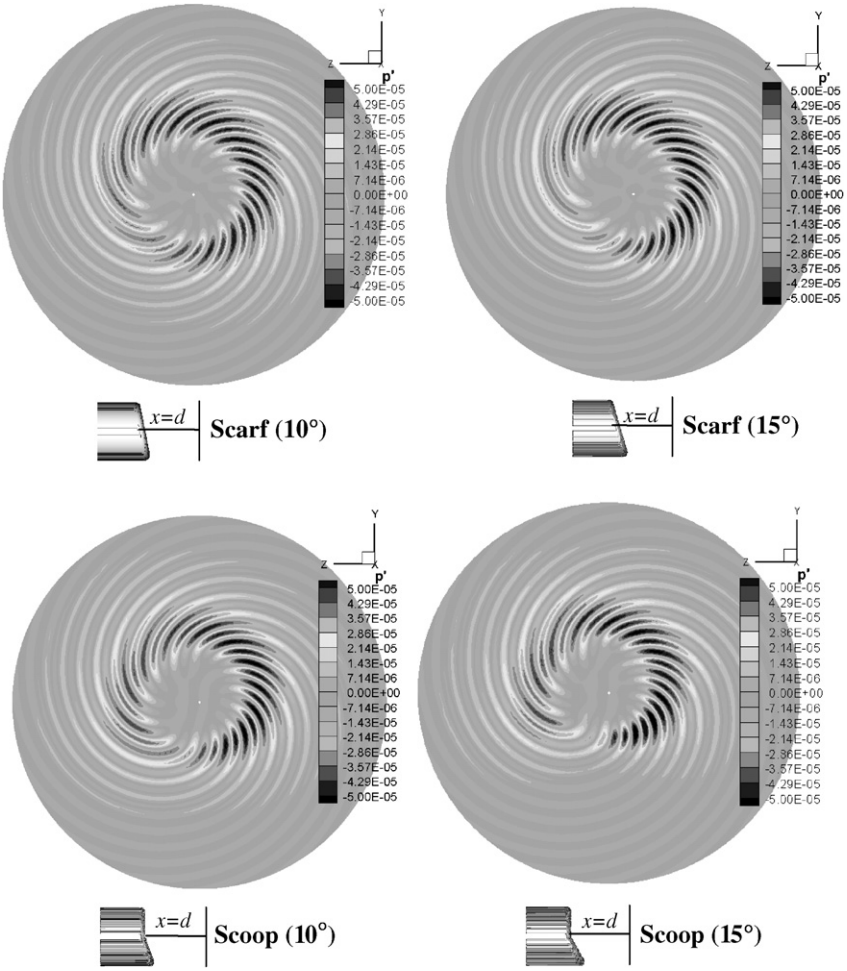

Fig. 10. Instantaneous pressure contour for each cases, at $x = d$ plane (d = diameter of aero-intake), $M_\infty = 0.0$.

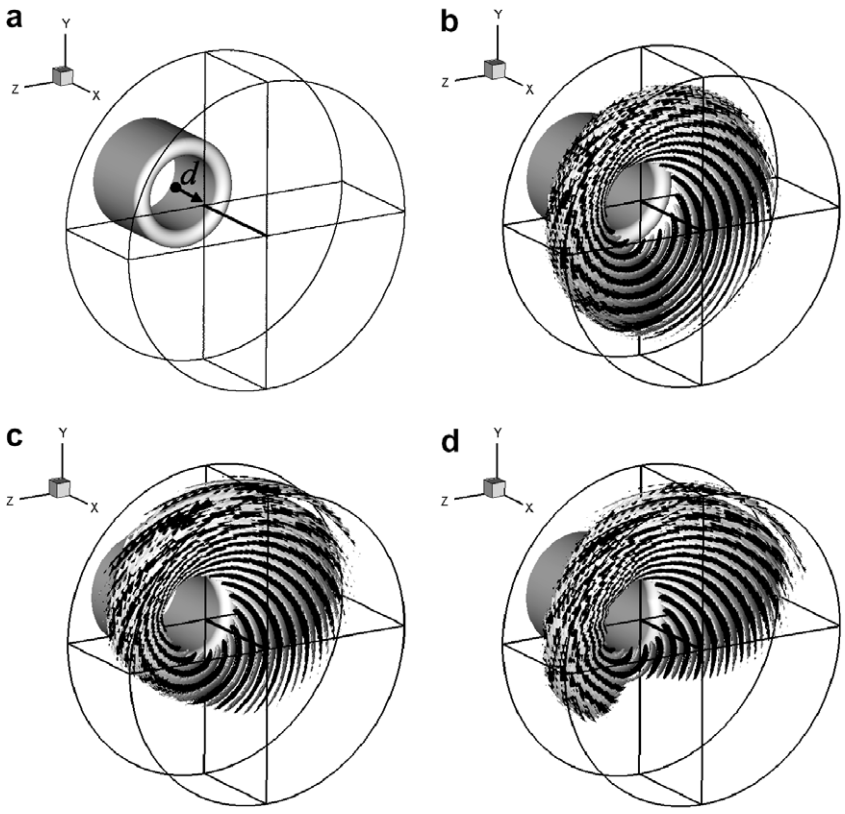

Fig. 11. Isobars of acoustic pressure, black-bars $= -1.0\times10^{-5}$, white-bars $= 1.0\times10^{-5}$, $T = 12.5$, $M_\infty = 0.0$; (a) view point, (b) axisymmetric intake, (c) scarf intake (15°), and (d) scoop intake (15°).

a vertex to a cone of rays with semi-angle, β which is an angle between the ray and the tangential direction of the edge of aero-intake. In case of the axisymmetric aero-intake, $\beta$of Keller's cone is constant along the circumferential location of the edge, and hence the sound radiation is symmetric. However, in case of the scarf and scoop aero-intakes, the wave propagation of swirling modes is not symmetric because β of Keller's cone is not symmetry, as shown in Fig. 12. Moreover, the larger β is near the lower part of the aero-intake, the more sound is diffracted toward ground and the ray which propagates downward (lower left part in this case) more affects the noise exposure on ground rather than the ray which propagates upward (right part of aero-intake).

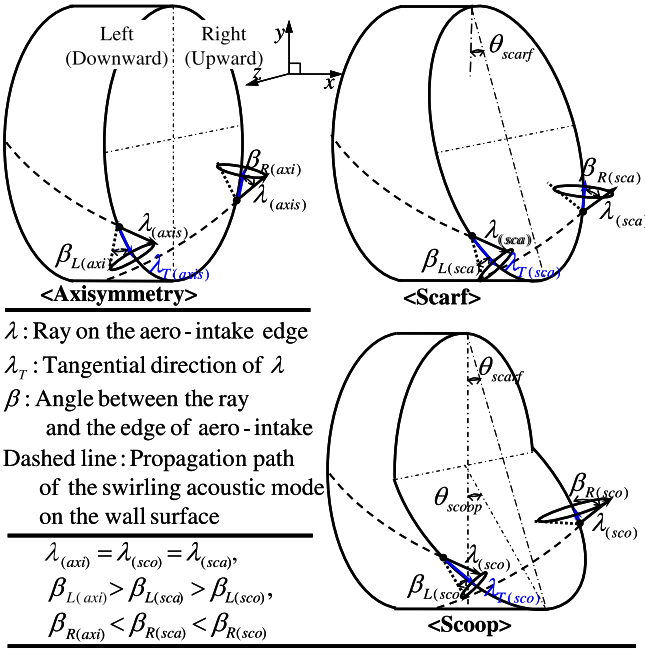

Fig. 12. Diffraction characteristics at the edge of each aero-intake.

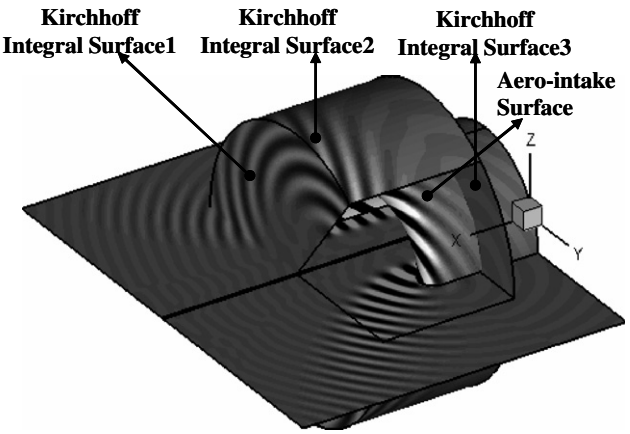

Fig. 13. Acoustic pressure contours on the Kirchhoff integral surfaces.

Therefore, the sound propagation from the scoop aero-intake is reduced toward ground since $\beta_{L(sco)}$ of scoop aero-intake is smaller than $\beta_{L(sca)}$ of scarf aero-intake under the same θ_{scarf}. This result also matches with isobars of acoustic pressure in Fig. 11 and the predicted far-field directivities shown in the following result. These highly three-dimensional, asymmetric characteristics of the scarf and the scoop engine should be fully considered to accurately predict the noise map associated with environmental noise regulations.

To predict far-field acoustic information, the Kirchhoff integral method was applied. The Kirchhoff integral surface was made up on the background Cartesian grid, which retains the same grid-resolution regardless of the distance from the duct, and thus allows the predicted values of the far-field acoustic pressure not sensitive to the locations of the integral surface. Fig. 13 shows the acoustic pressure contour at the Kirchhoff integral surfaces which are composed of three parts; the front circular plane, the cylindrical plane without a cover, and the back ring plane. They are fixed for all of the cases. The Kirchhoff integral time step (Δt_{kir}, is set to be $T_p/168$, where $T_p(=2\pi/\omega)$ is the period of the excited acoustic mode.

Fig. 14 present the predictions for the rms value of acoustic pressure, P_{rms}, at R_{ob} on the vertical plane (x–y plane) from the scarf and the scoop aero-intakes, respectively. The P_{rms} is normalized by the maximum P_{rms} of the axisymmetric aero-intake. It can be assured that, similar to the previous results, the lower extended part of the scarf and the scoop aero-intakes reflect the more acoustic

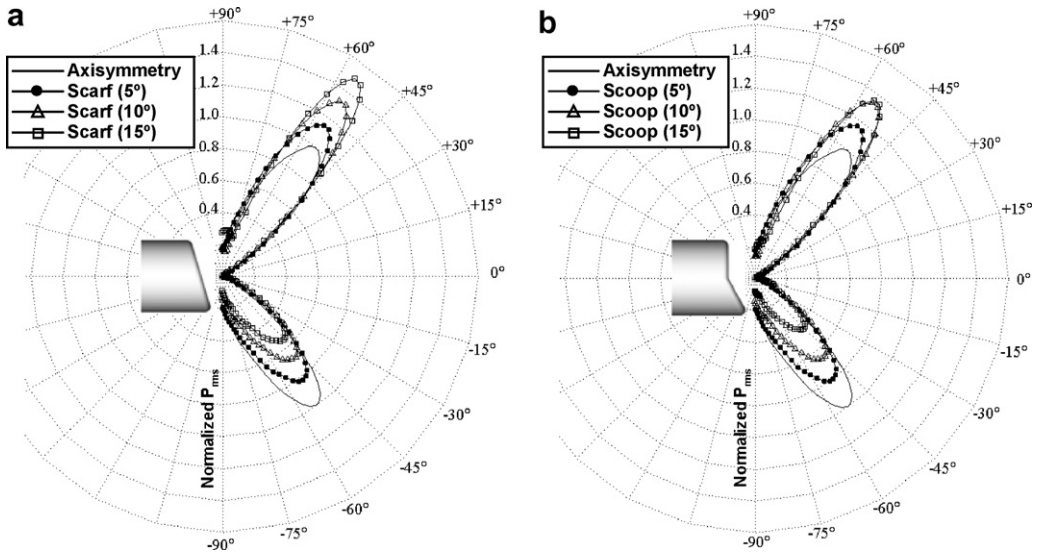

Fig. 14. Normalized P_{rms} and far-field directivity pattern in vertical plane (a) scarf (5°, 10°, and 15°) and (b) scoop (5°, 10°, and 15°).

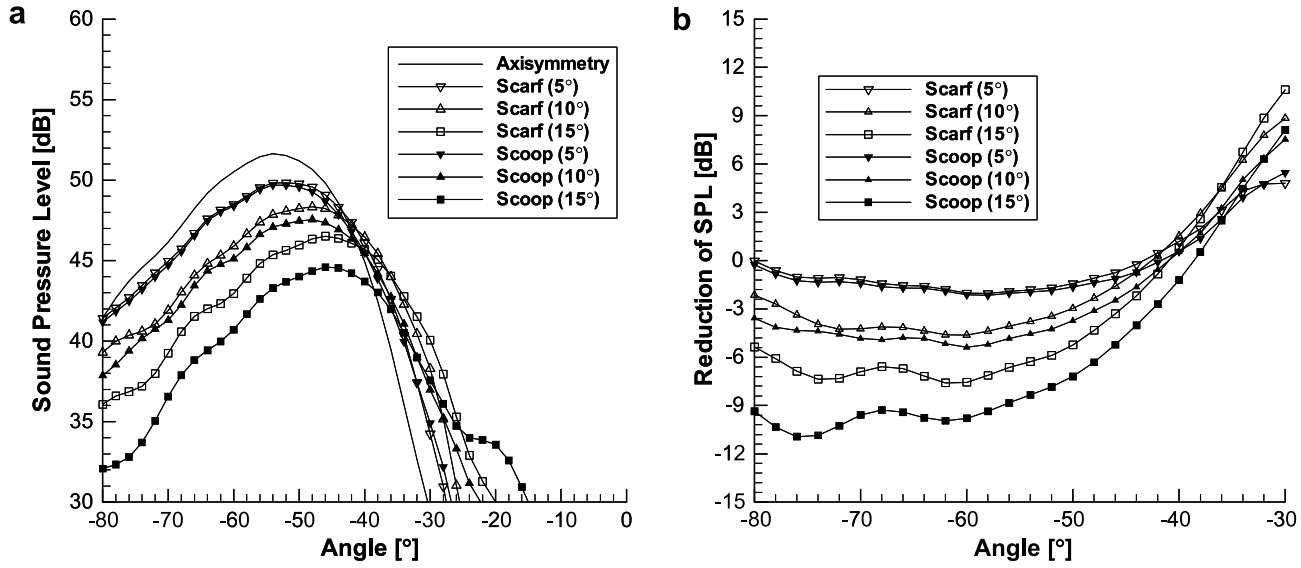

Fig. 15. Comparison of SPL toward ground for each case (a) SPL toward ground and (b) difference of SPL compared with axisymmetric aero-intake.

waves upward, and thus, the acoustic propagation into the ground direction is reduced. The peak radiation angle is also found to be slightly shifted upward with the increase of the scarf and the scoop angles. The peak radiation angle of the axisymmetric aero-intake, $\theta_{Pm\mu}$ is about $\pm 53°$, and agrees well with the result using the theoretical formulations [30]. It can be seen that the peak radiation angle toward ground is shifted by nearly $+6°$ for the scarf angle of 15°, compared with axisymmetric aero-intake. The effect of the scoop angles on the peak radiation angle is almost the same as the scarf angle.

For more quantitative comparison, the directivities toward ground in the vertical plane were compared with all of the cases. Fig. 15a compares the predictions of the sound pressure level with the common reference value, and Fig. 15b presents the differences in the sound pressure level between the scarf/scoop and the axisymmetric aero-intakes. It can be seen that the reduction of peak sound pressure level and the maximum reduction by the scoop aero-intake with the scoop angle of 15° are approximately 7 dB and 11 dB when compared with that of the axisymmetric aero-intake, while the scarf aero-intake with the scarf angle of 15° makes relatively less 5 dB and 7 dB reductions, respectively.

4.3. Mean flow effects

In this part, the effects of mean flow on the radiation of acoustic wave from the aero-intake are studied. The directivity of acoustic wave is often affected by its interaction with mean flow, which is essential to make a more reliable prediction of engine intake noise. This interaction may be theoretically explained by using the change of group velocity, the wave compression and expansion [30]. However, the actual phenomena occurring in the aero-intake is too complicated to be computed by using the theoretical approaches.

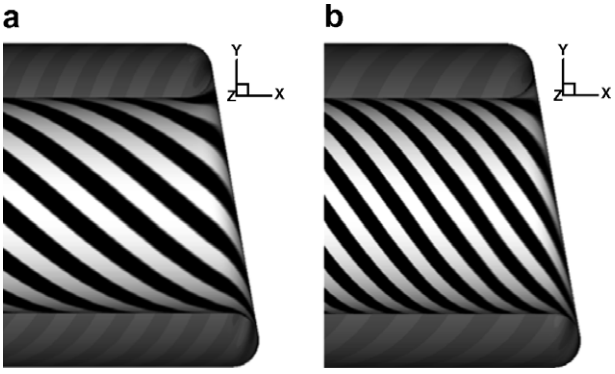

Fig. 16. Instantaneous acoustic pressure on the wall, angle of attack = 0° (a) scoop (10°), $M_\infty = 0.0$ and (b) scoop (10°), $M_\infty = -0.3$.

The mean flow property, i.e., the steady-state solution around the aero-intakes was obtained by numerically solving the Euler equations. The free flow velocity, M_∞, is set to be -0.3 with zero angle of attack.

Wave fronts propagating in the aero-intake of engine with the scarf angle of 10° are shown on the inner-surface of the aero-intake in Fig. 16, of which (a) and (b) present the results for the cases without and with mean flow, respectively. Comparing these two results shows that acoustic waves are compressed by intake mean flow. Here, the angle between the normal vector of local wave front and aero-intake axis, $\theta_{m\mu}$, decreases as the intake flow velocity increases, and as a result, the phase velocity vector is no more perpendicular to the wave fronts.

Fig. 17 shows the predictions of the acoustic pressure and steady pressure contours around the scarf aero-intake in the normal plane (x–y plane). It can be seen that the contours of background mean pressure is very complicated, especially near the lip of the aero-intake. It can be easily inferred from Fig. 17 that the propagation-direction and

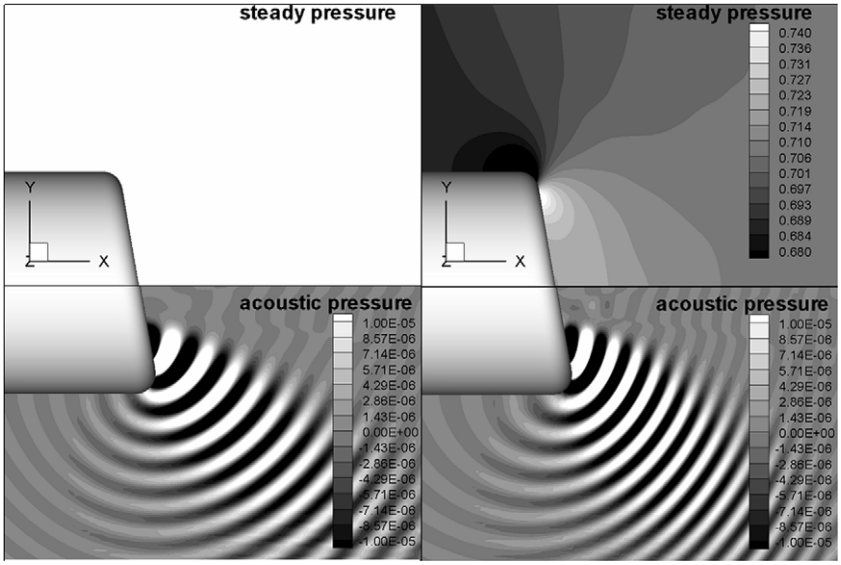

Fig. 17. Steady pressure contour and acoustic pressure contour outside the scarf (10°).

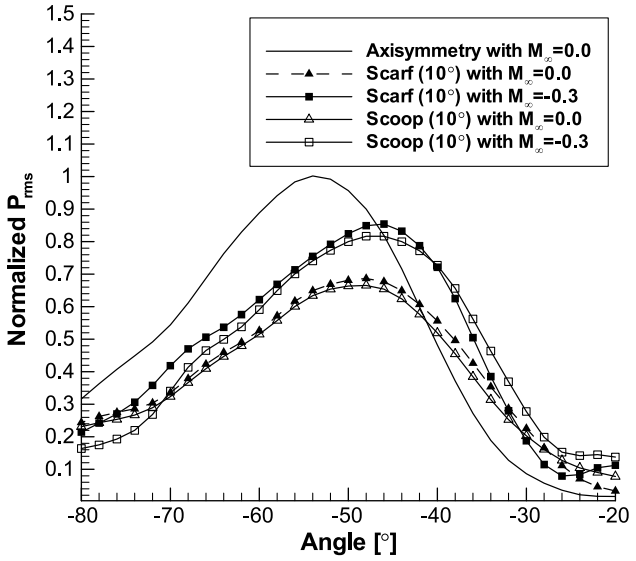

Fig. 18. Normalized P_{rms} with flow effect; scarf (10°) and scoop (10°).

the magnitude of acoustic waves are affected in complicated manner by the scattering of acoustic wave by the background mean flow, compared with the case of no mean flow. The general gross effect is that the wave fronts are more bent toward the x-axis and thus the group velocity vector is more bent toward the axial direction compared with no mean flow case.

Fig. 18 presents the comparison of the far-field normalized P_{rms} with and without mean flow effects. The shift of peak radiation angle by the flow has a reasonable agreement with the theoretical one [30]. The resulting overall peak radiation angle was shifted upward by about $+6°$ when compared with that of the axisymmetric aero-intake without mean flow. The peak radiation angle was shifted upward by about $+4°$ by the scarf (10°) effect as shown in the previous section. Therefore, the additional $+2°$ is resulted from the mean flow effects. Consequently, the peak radiation angle, $\theta_{Pm\mu}$, toward ground is about $-47°$. The predicted amplitudes of normalized P_{rms} for the both cases are increased with mean flow effects. The directivity patterns of acoustic wave from the scoop aero-intake show the trends similar to that of the scarf aero-intake.

Overall, whether the mean flow effect is or is not considered, the scoop aero-intake was found to be more effective than the scarf aero-intake in terms of the lower sound radiation toward ground. Besides, the scoop aero-intake has an advantage over the others in that its weight is lighter.

5. Conclusion

The radiation characteristics of the discrete-frequency noise from the scarf and the scoop aero-intakes were numerically analyzed using the high-order schemes for low dissipation and dispersion, the overset grid techniques for resolving the complicated geometries of the aero-intakes, and at same time, for retaining the grid-accuracy over the whole computation domain, the parallel computation to improve the speed of computation, and the Kirchhoff integral method to effectively predict the far-field directivity patterns.

It is shown that the 5 dB peak noise and the maximum 7 dB noise reductions can be achieved by using the scarf aero-intake with scarf angle of 15°, and the 7 dB peak noise and the maximum 11 dB noise reduction by the scoop aero-intake with the scoop angle of 15°, when compared with those by the axisymmetric aero-intakes. The peak lobe radiation angle toward ground was shifted upward by both the scarf and the scoop geometries and the mean flow. In addition, the amplitude of the acoustic pressure was slightly increased by its interaction with background mean flow.

Overall, the scoop aero-intake was seen to be more effective design than the scarf and the axisymmetric aero-intakes for the lower noise radiation toward ground, with the notice that the scoop aero-intake is lighter than the scarf aero-intake.

However, it was also found that the directivity pattern of the discrete-frequency noise from the scoop aero-intakes is highly three-dimensional, i.e., asymmetric, which also depend on the specific excited acoustic modes. If the scoop aero-intakes are used for the commercial aero-engines, these characteristics need to be analyzed in more detail.

Acknowledgement

This work is outcome of the fostering project of the Best Lab supported financially by the Ministry of Commerce, Industry and Energy (MOCIE) and supported by Grant No. (R01-2006-000-10301-0) from the Basic Research Program of the Korea Science & Engineering Foundation (KOSEF) in Korea.

References

[1] Dennis LH. Fan Noise Prediction: Status and Needs. NASA/TM-97-206533; 1997.
[2] Clark LR, Thomas RH, Dougherty RP, Farassat F, Gerhold CH. Inlet Shape Effects on the Far-field Sound of a Model Fan. AIAA Paper 97-1589; 1997.
[3] Abbott JM, Dietrich DA. Aerodynamic and directional acoustic performance of scoop Inlet. NASA Technical Paper 1028; 1977.
[4] http://www.grc.nasa.gov/WWW/RT/2004/RT/RTL-abbott.
[5] Baker NJ, Bewick CL. Noise test of a negative scarfed inlet flare. AIAA/CEAS aeroacoustics conference; 2001.
[6] Keith GM, Peake N. High-wavenumber acoustic radiation from a thin-walled scarfed cylinder. J Sound Vibrat 2002;255(1):129–46.
[7] Ozyoruk Y, Ahuja. Numerical simulation of fore and aft sound fields of turbofan. AIAA J 2004;42(10):2028–34.
[8] Ozyoruk Y, Long LN. Computation of sound radiating from engine inlet. AIAA J 1996;34(5):894–901.
[9] Bin J, Cheong C, Lee S. Optimized boundary treatment for curved walls for high-order computational aeroacoustics schemes. AIAA J 2004;42(2):414–7.
[10] Park Y, Bin J, Cheong C, Lee S. Simulation of trailing edge scattering by using acoustic/viscous splitting method with overset grid techniques.

Fourth Computational Aeroacoustics (CAA) Workshop on Benchmark; 2004.
[11] Cheong C, Ryu J, Lee S. Computation of aeolian tones from twin-cylinders using immersed surface dipole sources. J Mechan Sci Technol 2006;20(12):2292–314.
[12] Lyrintzis AS. Review: the use of the Kirchhoff's method's method in computational aeroacoustics. J Fluids Eng 1994;116:665–75.
[13] Farassat F, Myers MK. Extension of Kirchhoff's formula for radiation from moving surfaces. J Sound Vibr 1998;123:451–60.
[14] Ozyoruk Y, Long LN. A Navier-Stokes/Kirchhoff method for noise radiation from ducted fans. AIAA Paper 94-0462; 1994.
[15] Kim S, Cheong W, Park Y, Lee S. Prediction method for tire air-pumping noise using a hybrid technique. J Acous Soc Am 2006;119(6):3799–812.
[16] Tyler JM, Sofrin TG. Axial flow compressor noise studies. SAE Trans 1962;70:309–32.
[17] Tam CKW, Webb JC. Dispulsive-relation-preserving finite difference schemes for computational acoustics. J Comput Phys 1993;107(2): 262–81.
[18] Dong TZ, Povinelli LA. On computations of duct acoustics with near cut-off frequency. Second Computational Aeroacoustics (CAA) Workshop on Benchmark; 1996.
[19] Tam CKW, Dong TZ. Radiation and outflow boundary condition for direct computation of acoustics and flow disturbances in a nonuniform mean flow. J Comput Acous 1996;4(2):175–201.
[20] Tam CKW, Dong TZ. Wall boundary conditions for high-order finite difference schemes for computational aeroacoustics. Theoret Comput Fluid Dynam 1994;8:303–22.
[21] Cheong C, Lee S. The effects of discontinuous boundary conditions on the directivity of sound from a piston. J Sound Vibr 2001;239(3):423–43.
[22] Cheong C, Lee S. Grid-optimized dispersion-relation-preserving schemes on general geometries for computational aeroacoustics. J Comput Phys 2001;174:248–76.
[23] Heidmann MF, Saule AV, McArdle JG. Analysis of radiation patterns of interaction tones generated by inlet rods in the JT15D engine. AIAA paper 1979-581;1979.
[24] Gropp W, Lusk E, Skjellum A. Using MPI: portable parallel programming with the message passing interface. MIT Press; 1994.
[25] Rridge D, Becker D, Merkey P, Sterling T. Beowulf. Harnessing the power of parallelism in a pile-of-pcs. In: Proceedings, IEEE aerospace; 1997.
[26] Tam CKW. Computational aeroacoustics: methods and applications. AIAA short course; 1997.
[27] Ozyoruk Y, Sound radiation from ducted fans using computational aeroacoustics on parallel computer. Doctor of philosophy in Pennsylvania University; 1995.
[28] Eversman W, Parret AV, Preisser JS, Silcox RJ. Contributions to the finite element solution of the fan noise radiation problem. Trans ASME 1985;107:216–23.
[29] Keller JB. Geometrical theory of diffraction. J Optic Soc Am 1962;52:116–30.
[30] Joseph P, Nelson PA, Fisher MJ. Active control of fan tones radiated from turbofan engines. II. In-duct error sensors. J Acous Soc Am 1999;106(2):779–86.